

6. Optimizing Signal-to-Noise

Observations in the infrared require techniques to suppress the background emission reaching the detector as well as techniques to carefully remove the background emission from the signal. These considerations are critical for observations at thermal wavelengths, $\lambda \gtrsim 2.5 \mu\text{m}$.

We first discuss the signal-to-noise ratio (SNR) equation from which the effects of the background emission can be quantitatively judged. Then we discuss methods to suppress the background emission in hardware and software.

Notes:

6.1 The SNR equation.

Consider first the case of a single pixel. The noise components are assumed to add in quadrature, that is

$$\text{total noise} = \sqrt{\text{signal shot noise}^2 + \text{readnoise}^2 + \text{background}^2 + \text{dark current}^2}$$

If S is the number of signal electrons/sec measured by the detector and we assume Poisson statistics then the noise is $(S*t)^{0.5}$. This is referred to as "shot noise". In units of electrons, the SNR is

$$SNR = N_s / \sqrt{N_s + N_{rn}^2 + N_b + N_d}$$

where $N_s = (S*t)$, N_{rn} is the read noise for a pixel, $N_b = b*t$, $N_d = d*t$, and t is the integration time. b is the background rate per pixel (electrons/sec) and d is the dark current per pixel (electrons/sec). As we will see later, the read noise and dark current are much smaller than the background for imaging. The read noise can be significant for very fast readouts or for high-resolution spectrographs.

Notes:

In the case where the source is spread over n_p pixels and the total number of source electrons is N_T , the SNR equation is

$$SNR = N_T / \sqrt{N_T + n_p(N_{rn}^2 + N_b + N_d)}$$

This SNR equation is not complete since in a typical application we also have to subtract the background. For example in the case of photometry of a star, we need to measure the signal of the star and subtract off the background. The noise in the background pixels need to be taken into account. Following Merline and Howell (1995), we have:

$$SNR = N_T / \sqrt{N_T + n_p \left(1 + \frac{n_p}{n_b}\right) (N_{rn}^2 + N_b + N_d)}$$

where n_b is the number of background pixels used to estimate the background. In most cases $n_b \gg n_p$ and the prior SNR equation is a good approximation.

Notes: Reference: Merline, W. J. and S. B. Howell (1995). "A Realistic Model for Point-sources Imaged on Array Detectors: The Model and Initial Results." Experimental Astronomy 6: 163-210.

The SNR can now be worked out for an observation with a given exposure time and telescope size. If the science target has an intrinsic spectrum f_λ in units of $\text{W m}^{-2} \mu\text{m}^{-1}$, then the signal S in number of electrons per second is given by

$$\begin{aligned} S &= A \int (f_\lambda / h\nu) Q(\lambda) \tau_a(\lambda) d\lambda \\ &= A \int \lambda f_\lambda Q(\lambda) \tau_a(\lambda) d\lambda / hc \end{aligned}$$

where A is the telescope collecting area, τ_a is the atmospheric transmission, and Q is the overall throughput of the telescope, instrument, and detector. The integral is performed over the wavelength range of the filter passband or one resolution element of a spectrograph. For spectroscopy the above equation needs to account for the loss of light at the slit.

Notes:

In a similar fashion, the number of electrons per second in each pixel from a thermal background at a temperature T is given by

$$B = A\Omega \int \lambda \varepsilon(\lambda) B_\lambda(\lambda, T) Q(\lambda) d\lambda / hc,$$

where $B_\lambda(\lambda, T)$ is the blackbody function, $\varepsilon(\lambda)$ is the emissivity, and Ω is the solid angle viewed by a pixel. The sky background is estimated by

$$\varepsilon_s(\lambda) B_\lambda(\lambda, T),$$

where $\varepsilon_s(\lambda) = 1 - \tau_a(\lambda) = 1 - e^{-\tau(\lambda)}$ and $\tau(\lambda)$ is the optical depth of the telluric lines. The telescope background is estimated by $\varepsilon_t(\lambda) B_\lambda(T_{tel})$, where $\varepsilon_t(\lambda)$ is the emissivity of the telescope. In addition, OH emission from the sky is a bright non-thermal background source.

Notes:

The signal-to-noise equation shows that as long as the observations are not in the read noise limited or dark current limited regime (i.e., $N_b \gg N_m$ and $N_b \gg N_d$), then

$$\begin{aligned} SNR &= N_T / \sqrt{N_T + n_p N_b} \\ &= St / \sqrt{St + n_p bt} \end{aligned}$$

and the SNR increases as the square root of the telescope area or the exposure time.

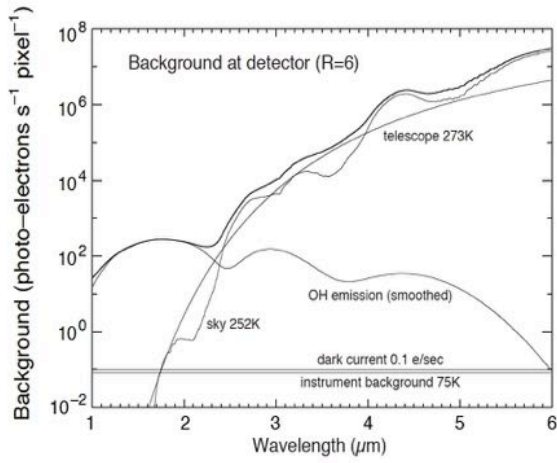
For most mid- and far-IR observations (especially from the ground), we have $N_b \gg N_T$, which is the background-limited case. In this case, $SNR = N_T / \sqrt{n_p N_b}$ and the SNR increases linearly with the source flux. For example, at 10 μm , the photon flux from a 1 Jy source is approximately $1.5 \times 10^6 \text{ photons s}^{-1} \text{ m}^{-2} \mu\text{m}^{-1}$, while the sky background emits $3.6 \times 10^9 \text{ photons s}^{-1} \text{ m}^{-2} \mu\text{m}^{-1}$ in 1 arcsec^{-2} , a factor of over 2,000 times larger.

Notes:

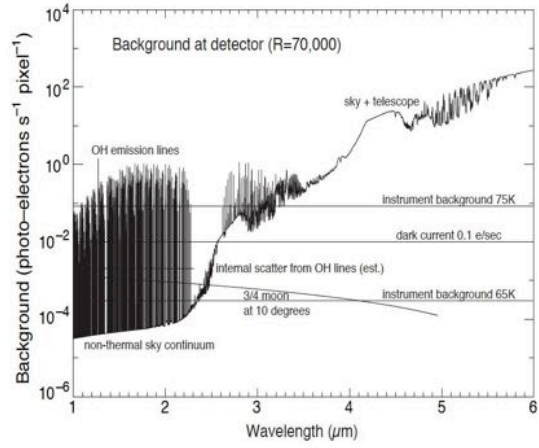
Inspection of the figure on slide 3-17 shows that the background emission from the sky and telescope completely dominates the detector dark current for imaging and low resolution spectroscopic observations. To maximize the SNR, the array is exposed long enough so that shot noise from the background is larger than the read noise. Current near-IR arrays have a read noise of as low as about 3-5 electrons, so integration times of a few seconds are sufficient to be background limited with broadband imaging at wavelengths $> 1.2 \mu\text{m}$.

The situation is very different for high-resolution spectroscopy. In the example shown in the figure on slide 3-18, the background levels are extremely low in between the OH emission lines. Here one would set the exposure for as long as possible before reading out the array as long as higher noise can be tolerated at the positions of the OH lines. If the array is very stable, long integrations of 600–1,200 s are possible at $1\text{--}2.5 \mu\text{m}$.

Notes:



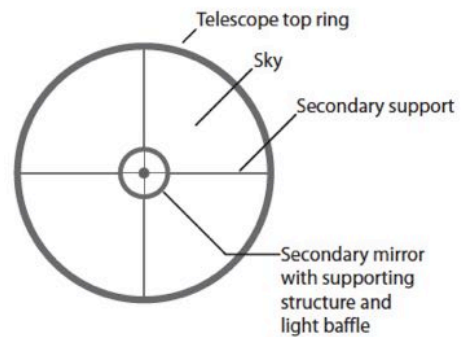
Slide 3-17



Slide 3-18

6.2 IR-optimized telescopes

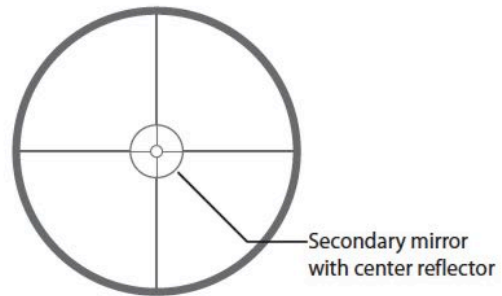
Various methods have been developed to reduce the thermal background of telescopes. To visualize what the detector sees, it is instructive to imagine putting your eye at the focus of a telescope. Looking up at the secondary mirror, you would see the secondary mirror itself, the supporting structure behind the secondary mirror, the secondary mirror spiders, the sky behind the secondary mirror, and the telescope top ring holding the secondary mirror in place (see figure). An instrument working at thermal IR wavelengths ($\lambda > 3 \mu\text{m}$) would see thermal emission from all of these surfaces. Even the primary and secondary mirrors would be thermally emitting surfaces. The sky would be radiating thermally. Any light baffles would be a major source of thermal emission as well.



High emissivity surfaces are shown in dark color. Note that the hole in the primary mirror is a region of high emissivity.

Notes:

An IR-optimized telescope is designed to keep all radiating surfaces to a minimum, as shown in this figure. The secondary mirror supporting structure is constructed to be completely behind the secondary mirror. The secondary mirror is undersized so that highly emissive mirror cell is not seen. There are no light baffles; stray light control is designed into the instrument. There is a conical mirror at the center of the secondary mirror to block thermal emission arising from the central hole in the primary mirror. Low emissivity coatings such as over coated silver are used on the primary and secondary mirrors. Some or all of these features are designed into telescopes such as the 3.8-m United Kingdom Infrared Telescope, the 3.0-m NASA Infrared Telescope Facility (IRTF), and the 8.0-m Gemini North telescope.



View of an IR-optimized telescope. The secondary mirror is undersized and there is a conical mirror to reflect the sky as see by the detector. The secondary structure is hidden behind the secondary mirror.

Notes: The IRTF has an $f/38$ secondary mirror, which reduces the central obscuration of the primary mirror and this minimizes the thermal emission from the telescope. The Gemini North telescope employs overcoated silver (Boccas et al. 2004; Vucina et al. 2006) so that the emissivity is about 2% per mirror surface in the near infrared and about 1.4% in the mid infrared. This can be compared to >25% for the total emissivity for a conventional telescope.

References: Boccas, M. et al. (2004). Coating the 8-m Gemini telescopes with protected silver. *SPIE*, **5494**: 239-253.
Vucina, T. et al. (2006). Gemini's protected silver coatings: first two years in operation. *SPIE*, **6273**: 62730W.

IRTF secondary mirror with reflective center button.

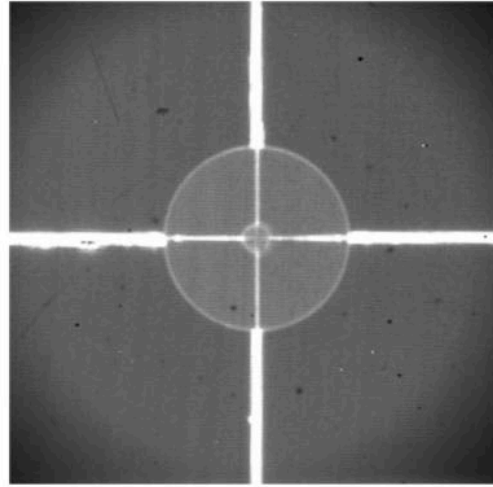


A. Tokunaga, Introduction to Infrared Astronomy, Univ. of Tokyo
Visiting Professor Lecture, Feb. 2018

6-11

This figure shows a thermal image of the IRTF secondary mirror taken at $3.3\ \mu\text{m}$. The thermal emission from the primary mirror, secondary mirror, and spiders are emitting toward the detector. The supporting structure for the secondary mirror is completely behind the secondary mirror. There are no light baffles in the telescope.

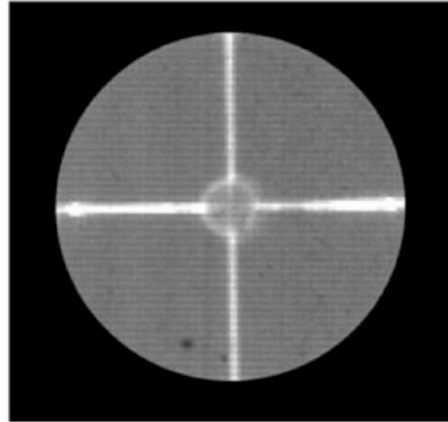
The sky and the reflection of the sky in the secondary mirror are much colder than the secondary spiders. The emission from the hole in the primary mirror is reflected away by a reflecting mirror centered on the secondary mirror.



Notes:

All IR instruments are designed to have a cold pupil stop within the instrument. At this stop there is an image of the secondary mirror, and if, necessary, a cold mask can be located here to block the thermal emission from the spiders, the hole in the primary mirror, and any warm light baffles. Such measures are often taken with optical telescopes that have high emissivity.

This figure shows the pupil image of the secondary mirror of the IRTF. The background emission from the environment is limited to the sky, spiders, telescope mirrors, and the warm instrument window. Low emissivity coatings on the telescope mirror and keeping the mirrors clean will minimize emission from the telescope.



Notes: Telescopes at the South Pole take advantage of the much lower temperatures of both the sky and the telescope (Burton 2010). SOFIA accomplishes this to a much greater degree by going to an altitude of 14 km.

Reference: Burton, M. G. (2010). "Astronomy in Antarctica." *Astronomy and Astrophysics Review* **18**: 417-469.

6.3 Data Taking Techniques for Reducing the Background

Although every attempt is made to reduce the sky, telescope, and instrument background, the background levels are still very high compared with most astronomical objects. Therefore, background subtraction techniques have been developed to maximize the signal-to-noise ratio.

6.3.1 Near-infrared Imaging

Time variability of the IR background requires frequent measurements of the telescope and sky background. Depending on the site and wavelength, imaging exposure times can be as short as a few minutes due to the highly variable OH emission at 1-2.5 μm . At longer wavelengths the variability of the telluric emission lines, as well as quick saturation of the pixels by the huge number of photons detected, requires much shorter integration times. At 10 μm the exposure times of individual frames is about tens of milliseconds.

Notes: Special handling of data is always required due to problems arising from array defects and array readout characteristics, fringing effects arising from the array, instrumental effects (scattered light, nonuniform illumination), and variable weather.

References: McLean, I. (2008). Electronic Imaging in Astronomy: Detectors and Instrumentation, 2nd edition. New York, Springer.

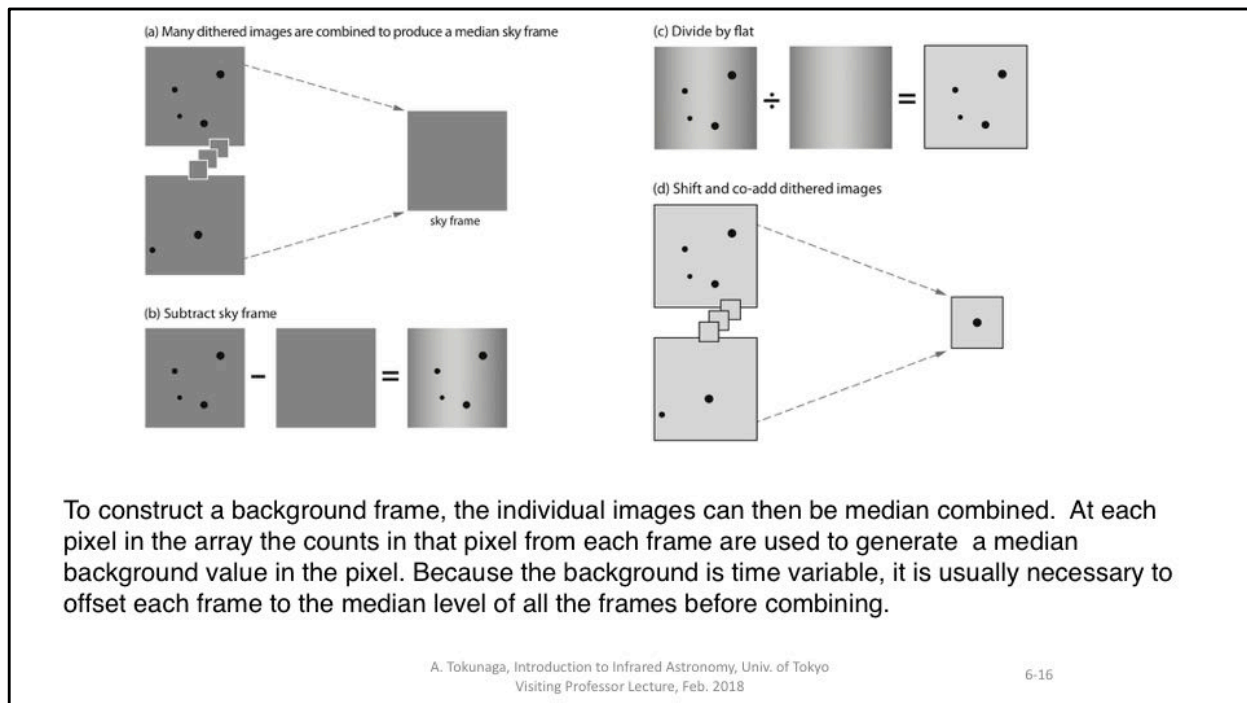
To understand the steps employed in the reduction of IR data, it is useful to begin by writing the equation for the number of counts detected at a given pixel i in an array:

$$I_i^{obs} = F_i(S_i + B_i) + D_i$$

where S_i is the signal from the source, B_i is the background, and D_i is the dark current. F_i is the relative response of the pixel (from the “flat field” image).

For the near-IR regime, in which the thermal background is relatively stable, a background frame is often generated as part of the observations from “dithered” observations. These consist of multiple exposures of the source, with the telescope moved slightly between each observation. The amount of each move, or dither, depends on the expected extent of the sources as well as the need to avoid bad regions of the array. The latter may consist of clusters of bad pixels or regions of low quantum efficiency (QE).

Notes:



Notes: Steps in removing the background. First a median sky frame is produced (step a). Because the background is time variable, it is usually necessary to offset the background image by a constant factor equal to the difference in the median values between the source frame and the background image before subtraction. The result should yield a “background subtracted” image with a median level around zero.

Then the sky frame is subtracted from each exposure (step b). To remove variation in the pixel response, the image is divided by a flat field (step c). The ideal flat field is obtained by observing a uniformly illuminated source that fills the telescope beam exactly like the astronomical source.

In the final step the images are shift and added to make a final image frame (step d).

The flat-field F_i can be obtained from the background frames if the count levels in the sky background are large enough. The background frames are normalized by the mean, median, or modal values in each frame and then median combining them. Dithered observations of blank sky at twilight can also be used to generate flat fields. In both cases, using observations to produce flat fields assumes that the background is uniform across the array.

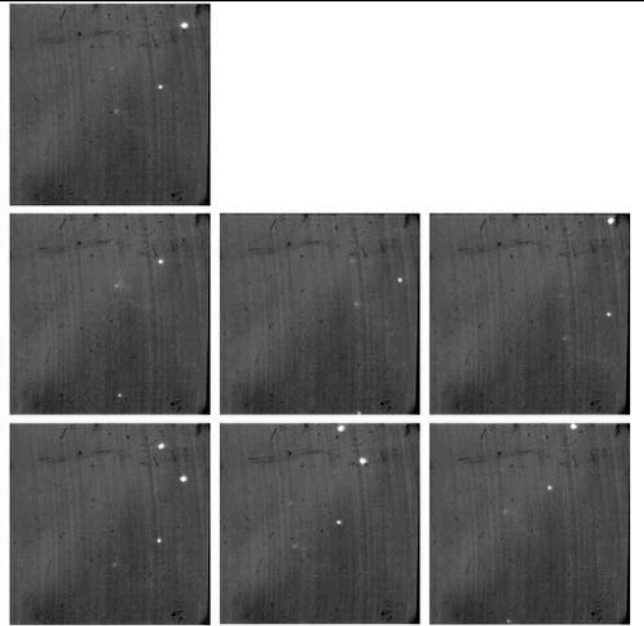
The dark current at each pixel should be subtracted from flat field frames. The dark current image can be generated by averaging frames taken with the detector blocked from all light. These frames should have the same exposure times as the background frames used to generate the flat fields. However, for most near-IR arrays, the contribution to the detected counts due to dark current is negligible compared with that from other background sources.

The most effective way to obtain the flat field must be determined empirically, since the instrument and telescope characteristics vary and the method used depends on the wavelength and whether imaging or spectroscopy is being done. In general flat fields are never perfect and the processing of data need to take this into account.

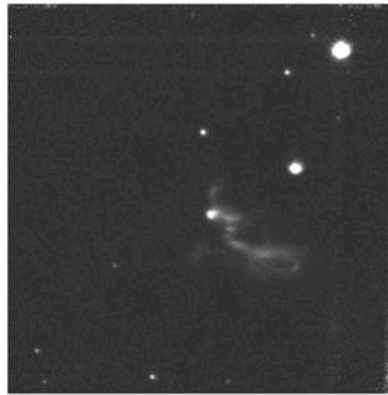
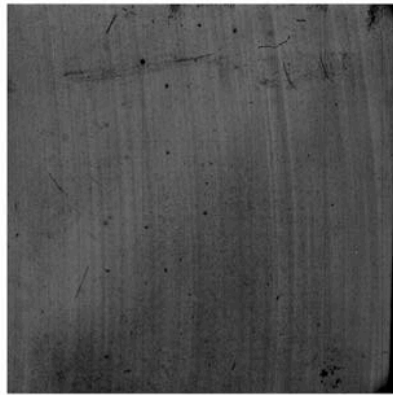
Notes: Naylor (1998) discusses ideas for optimizing the SNR in photometry. He points out that each source frame must be processed with its own unique background and flat images, generated from all the other source frames. As stated by Naylor (1998, p. 342), "Each frame must be flat-fielded with the median of all the frames in the group excluding itself."

Reference: Naylor, T. (1998). "An optimal extraction algorithm for imaging photometry." Monthly Notices of the Royal Astronomical Society **296**: 339-346.

Seven-point dither images. Dither pattern is in the shape of a hexagon with one image in the center of the hexagon (top row). Image was taken with the slit viewer of SpeX on the NASA IRTF.



Notes: Images from M. Connelley, private communication.



(Left) Sky image generated from a median co-addition of the dithered images in the previous slide.
(Right) Final image obtained by subtracting the sky image and realigning and coadding the dithered images

Notes:

Typical problems with IR arrays

Problem	Remedy
Nonuniform quantum efficiency	Divide by flat field
Bad pixels; cosmic-ray hits	Mask or filter out by dithering
Dark current and hot pixels	Remove by sky subtraction
Nonlinearity	Stay within linear range or apply linearity correction
Latent images	Avoid bright sources or saturation before exposing on faint sources
High background	Dither to get sky frame

Many of the effects in the table be reduced to an acceptable level by dithering and by taking the object and calibration exposures with the same settings.

Near-IR arrays are inherently nonlinear because of the method used to sense the number of photoelectrons generated by the detector. The nonlinearity for each pixel can be measured and a correction factor applied (McLean 2008; Vacca et al. 2004). In most cases observations are made only in the linear range of the detector.

Bright sources create latent images in near-IR arrays that arise from “charge trapping” in the readout amplifier (Solomon et al. 1993). Modern IR arrays have minimal latent images. However latent images cannot be entirely suppressed, and this effect should be considered in how the data are taken and reduced.

Notes:

6.3. Mid-infrared Imaging

A room temperature blackbody peaks near 10 μm so that every warm surface is bright in the infrared. The sky emission is up to 10^6 brighter than the celestial background and is highly variable due to variations in the atmospheric constituents such as water vapor.

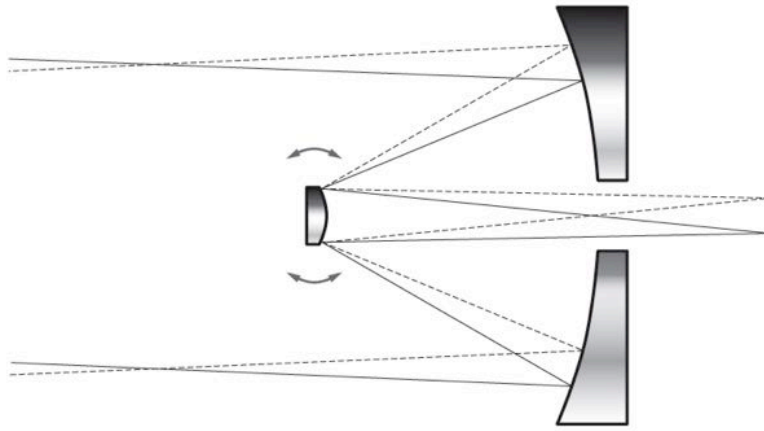
Low and Rieke (1974) introduced the "sky chopping" technique of temporally modulating the sky emission on the detector by using a chopping secondary mirror (see slide 6-20). This allows rapid removal of the sky emission at 1–10 Hz and it can reduce the low-frequency sky noise by a factor of 10^3 – 10^4 . The optimum frequency and amplitude of the sky chopping depends on the sky conditions and must be determined empirically (Papoular 1983; Kaeufl et al. 1991; Miyata et al. 2000; Mason et al. 2008).

For a point source, a chop frequency of 10 Hz and amplitude of 0.5–1 arcmin is typical, although the chop amplitude is larger at far-IR wavelengths due to the larger beam size. The smallest chop amplitude possible should be used to minimize differences in the sky or telescope emission.

Notes: In an early primer on IR photometry, Low and Rieke (1974, p. 444) stated, "Observing at 10 μm with a ground-based telescope has been likened to observing visually through a telescope lined with luminescent panels and surrounded by flickering lights as though the telescope dome were on fire." This is literally true.

References:

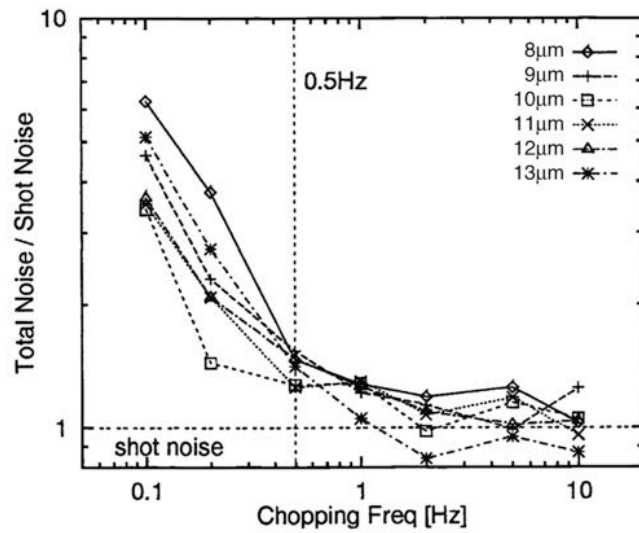
- Kaeufl, H. U. et al. (1991). "A sky-noise measurement and its implication for ground-based infrared astronomy in the 10-micron atmospheric window." *Experimental Astronomy* 2: 115-122. . [Empirical data on sky noise.]
- Low, F. J. and G. H. Rieke (1974). The instrumentation and techniques of infrared photometry. *Methods of Experimental Physics: Optical and infrared*. N. P. Carleton. New York, Academic Press. Vol. 12A: 415-462.
- Mason, R. et al. (2008). Observing conditions and mid-IR data quality. *SPIE*. 7016: 70161Y. . [Empirical data on sky noise.]
- Miyata, T. et al. (2000). Mid-infrared camera and spectrometer (MICS) and sky noise measurement in the N-band. *Proc. SPIE*. Bellingham, WA, SPIE. 4008: 842-852. [Empirical data on sky noise.]
- Papoular, R. (1983). "The processing of infrared sky noise by chopping, nodding and filtering." *Astronomy and Astrophysics* 117: 46-52. [Good discussion of the physics underlying sky noise.]



Sky Chopping. The secondary is oscillated, producing two images in the focal plane. Subtraction of these images eliminates most of the low frequency noise components. Note that the secondary mirror must be undersized so that the edge of the beam on the primary mirror does not reach warm surfaces of the mirror cell

Notes: Sky chopping is necessary only at mid-IR wavelengths ($\lambda \gtrsim 5\mu\text{m}$).

Example of sky noise showing frequency and wavelength dependence of sky noise. “1/f” noise dominates at low frequencies and arises from sky emission fluctuations and detector noise. The sky noise depends on the wavelength, with higher noise at wavelengths where thermal emission from water vapor is high. This data taken at Mauna Kea shows that the sky subtraction should be done at a frequency $\geq 0.5\text{Hz}$. From Miyata et al. (2000).



Notes: The variability of the sky background is the main problem, not the absolute magnitude of the background.

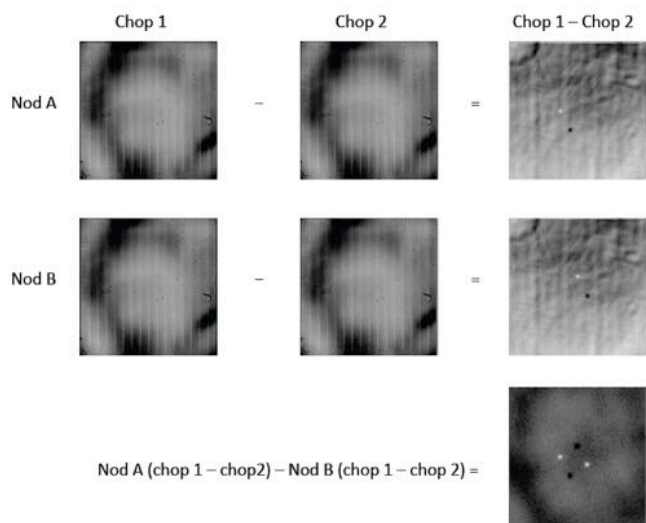
The optimum sky subtraction frequency is dependent on the site, the detector used, and local sky conditions during the observations.

Although sky chopping eliminates most of the variable sky emission, there is an offset signal that arises from small temperature imbalances on the telescope optics and structure. To remove this offset signal, the telescope is moved or “nodded” to a different location on the sky. The difference between the first and second positions removes the unwanted offset signal.

For point sources, chopping and nodding amplitudes are usually small enough such that the object remains on the detector during both chopping and nodding. For extended sources, however, it is often necessary to chop off the object to a sky region and to nod the telescope to another sky region.

Notes:

Example of the sky emission from mid-IR imaging data. The four images on the left are raw frames of a standard star (γ Dra) obtained at 24 μm with the FORCAST instrument on SOFIA (Herter et al. 2013). The final image at the lower right is the result of subtracting the chopped images at each nod position (chop subtraction) and then subtracting the two chop-subtracted images at the two nod positions (nod subtraction). This double subtraction removes the sky background emission as well as the offset residual due to the telescope. No flat fielding has been applied.



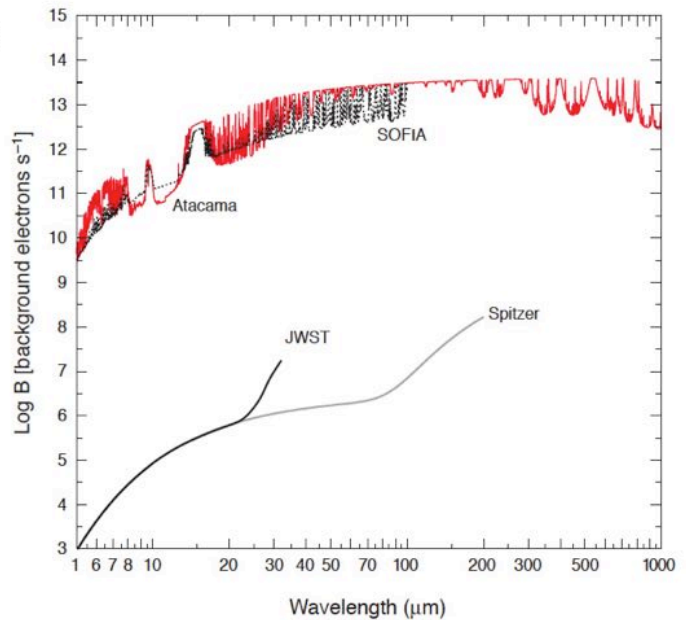
Notes: Each frame represents the sum of $\sim 6,000$ integrations, each ~ 2 ms, for a total integration time of ~ 12 s at one of the two chop positions (1 and 2) and one of the two nod positions (A and B). The chop throw was 30 arcsec, and the chop frequency was ~ 4 Hz.

Flat fielding was not successful with this instrument and telescope, and so it is necessary to have many observations so that the average background level could be obtained.

Reference: Herter, T. L. et al. (2013). "Data Reduction and Early Science Calibration for FORCAST, A Mid-Infrared Camera for SOFIA." *Publications of the Astronomical Society of the Pacific* **125**: 1393. [This paper describes details of data taking, removal of detector non-linearity and other effects, and calibration. The full complexity of data taking and reduction can be appreciated by reading this paper.]

6.4. Airborne and Space Observatories

The total backgrounds for the very best Atacama conditions (precipitable water vapor 0.2 mm and seeing of 0.25 arcsec) compared with SOFIA, JWST, and Spitzer. Assumed temperatures of Atacama (red solid line), SOFIA (black dashed line), JWST, and Spitzer are 260, 240, 40, and 5.5 K, respectively. SOFIA flies above 12-km altitude. For the JWST, the background is set by zodiacal emission except beyond 20 μm where the telescope emission becomes important. Note the calculation for SOFIA does not go beyond 100 μm . Adapted from Giovanelli et al. (2001).



A. Tokunaga, Introduction to Infrared Astronomy, Univ. of Tokyo
Visiting Professor Lecture, Feb. 2018

6-26

Notes: The 6 orders of magnitude difference in background means that even modest-sized space-based observatories like IRAS, Spitzer, and WISE can be up to 10^3 times more sensitive than ground-based facilities.

Reference: Giovanelli, R. et al. (2001). "The Optical/Infrared Astronomical Quality of High Atacama Sites. II. Infrared Characteristics." *Publications of the Astronomical Society of the Pacific* **113**: 803-813.

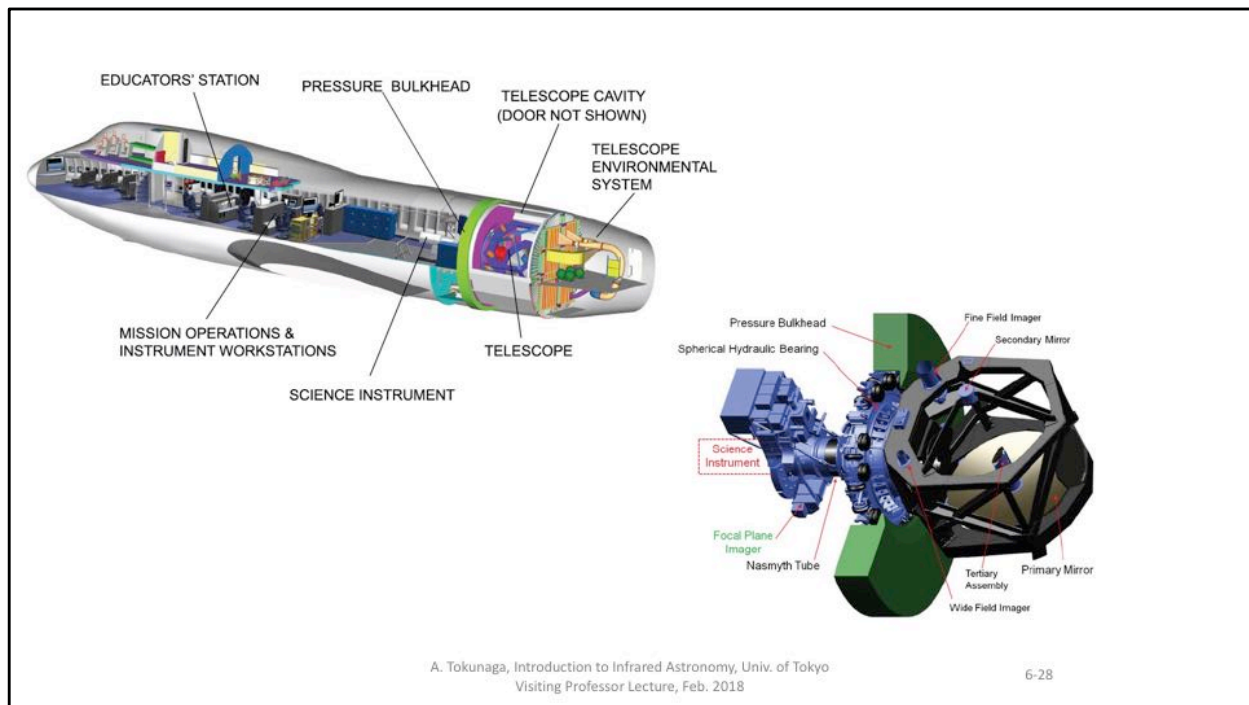
SOFIA - Stratospheric Observatory for Far-IR Astronomy
- 2.7 m telescope
- 14 km operating altitude



A. Tokunaga, Introduction to Infrared Astronomy, Univ. of Tokyo
Visiting Professor Lecture, Feb. 2018

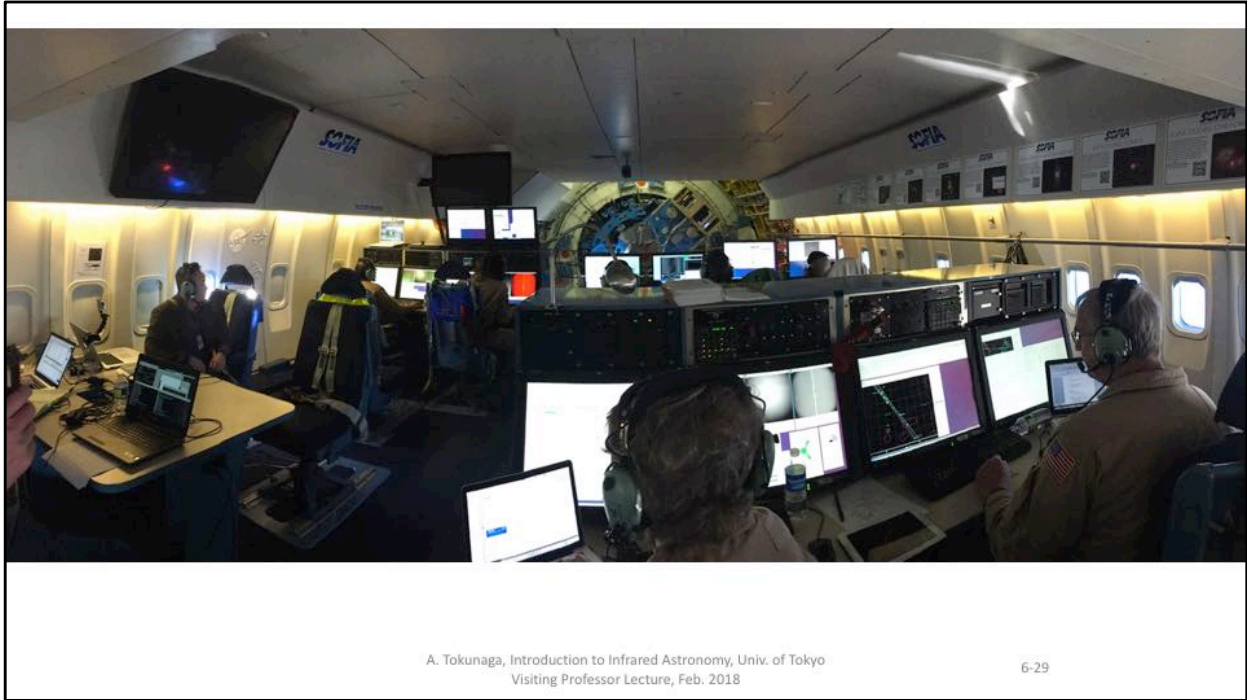
6-27

Notes: <https://www.sofia.usra.edu/>
<https://www.sofia.usra.edu/sites/default/files/SOFIAtech2016.pdf>



The telescope is at the rear of the aircraft. A pressure bulkhead keeps the cabin of the aircraft sealed from the outside air. An air bearing allows the telescope to track objects in the sky while the aircraft deviates due to turbulence.

Young, E. T. et al. (2012). "Early Science with SOFIA, the Stratospheric Observatory For Infrared Astronomy." The Astrophysical Journal Letters **749**: L17.



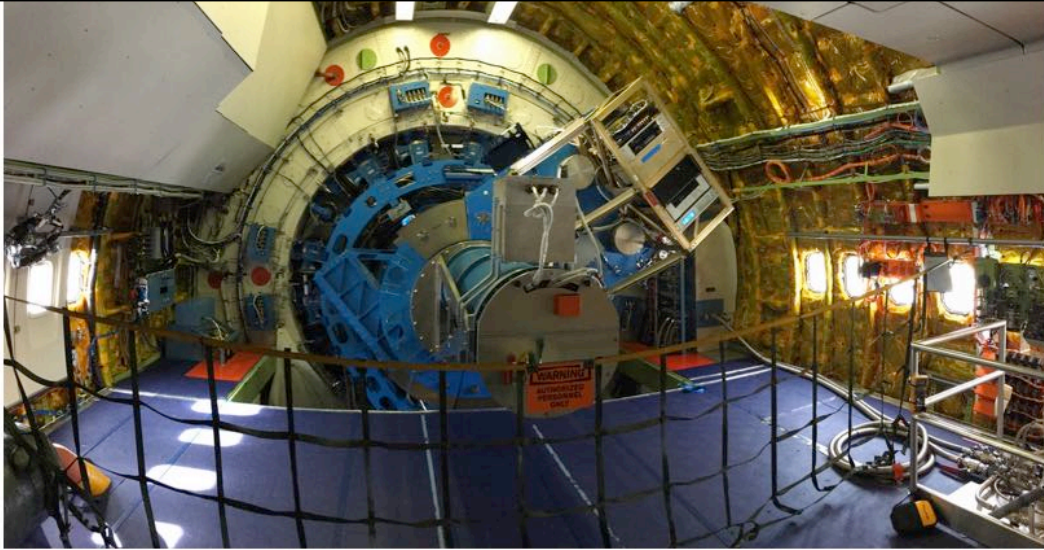
A. Tokunaga, Introduction to Infrared Astronomy, Univ. of Tokyo
Visiting Professor Lecture, Feb. 2018

6-29

Interior view of SOFIA while observing. The instrument is in the back of the photo. The mission director is in the foreground. The observer can be present while data is being taken.



View of the instrument. The observing team is facing the instrument.



A. Tokunaga, Introduction to Infrared Astronomy, Univ. of Tokyo
Visiting Professor Lecture, Feb. 2018

6-31

Instrument mounted to the telescope. This is the TEXES instrument for observing at high spectral resolution in the mid-IR (M. Richter, PI).

Selected Space Infrared Missions						
Mission	Launch	Aperture (m)	Instruments	Function	Wavelength (μm)	Reference
IRAS	1983	0.6	62 detectors DAX	All-sky survey spectrometer	12, 25, 60, 100 7.5–23	Neugebauer et al. (1984)
COBE	1989	0.6	DIRBE FIRAS DMR	IR radiometer FTS spectrometer Microwave radiometer	1.25–240 0.1–10 mm 3.3, 5.6, 9.3 mm	Boggess et al. (1992)
ISO	1995	0.6	SWS LWS ISOCAM ISOPHOT	Spectrometer Spectrometer Camera Photometer	2.4–45 45–197 2.5–17 2.5–240	Kessler et al. (1996)
MSX	1996	0.35	SPIRIT III	6-channel radiometer	4.3–21.3	Egan et al. (1999)
HST	2002	2.4	NICMOS w/cryocooler	Camera	0.8–2.5	Viana et al. (2009)
Spitzer	2003	0.85	IRAC MIPS IRS	Camera Imaging photometer Spectrometer	3.6, 4.5, 5.8, 8.0 24, 70, 160 5.2–38	Werner et al. (2004)
Akari	2006	0.68	IRC FIS	Infrared camera Far IR surveyor	2.4–24 65, 90, 140, 160	Murakami et al. (2007)
HST	2009	2.4	WF3/ IR	Camera	0.8–1.7	Dressel (2011)
Herschel	2009	3.5	PACS SPIRE HIFI	Photometer/spectrometer Photometer/spectrometer Heterodyne spectrometer	60–210; 51–220 250, 350, 500; 157–212; 240–625	Pilbratt et al. (2010)
Planck	2009	1.9 × 1.5	LFI HFI	Radiometer Radiometer	4.3–10 mm 0.35–3 mm	Planck Collaboration et al. (2011a)
WISE	2009	0.4	4 Arrays	All-sky survey	3.4, 4.6, 12, 22	Wright et al. (2010)
JWST	2018	6.5	NIRCam NIRSpec MIRI	Camera spectrometer Camera/spectrometer	0.6–5 0.6–5 5–28	Gardner et al. (2006) Clampin (2011)

Notes: I will return to discuss some of these space missions in more detail.

Boggess, N. W. et al. (1992). "The COBE mission - Its design and performance two years after launch." *The Astrophysical Journal* **397**: 420-429.

Clampin, M. (2011). Overview of the James Webb Space Telescope observatory. *SPIE*. **8146**: 814605.

Dressel, L. (2011). "Wide Field Camera 3 Instrument Handbook", Version 4.0, Space Telescope Institute.

Egan, M. P. et al. (1999). "The Midcourse Space Experiment Point Source Catalog Version 1.2 Explanatory Guide." *Air Force Research Laboratory Technical Report AFRL-VS-TR-1999-1522*.

Gardner, J.P. et al. (2006). "The James Webb Space Telescope." *Space Science Reviews* **123**: 485-606.

Kessler, M. F. et al. (1996). "The Infrared Space Observatory (ISO) mission." *Astronomy and Astrophysics* **315**: L27-L31.

Murakami, H. et al. (2007). "The Infrared Astronomical Mission AKARI." *Publications of the Astronomical Society of Japan* **59**: 369.

Neugebauer, G. et al. (1984). "The Infrared Astronomical Satellite (IRAS) mission." *The Astrophysical Journal Letters* **278**: L1-L6.

Pilbratt, G. L. et al. (2010). "Herschel Space Observatory. An ESA facility for far-infrared and submillimetre astronomy." *Astronomy and Astrophysics* **518**: L1.

Planck_Collaboration, P.A.R. Ade, et al. (2011). "Planck early results. I. The Planck mission." *Astronomy and Astrophysics* **536**: A1.

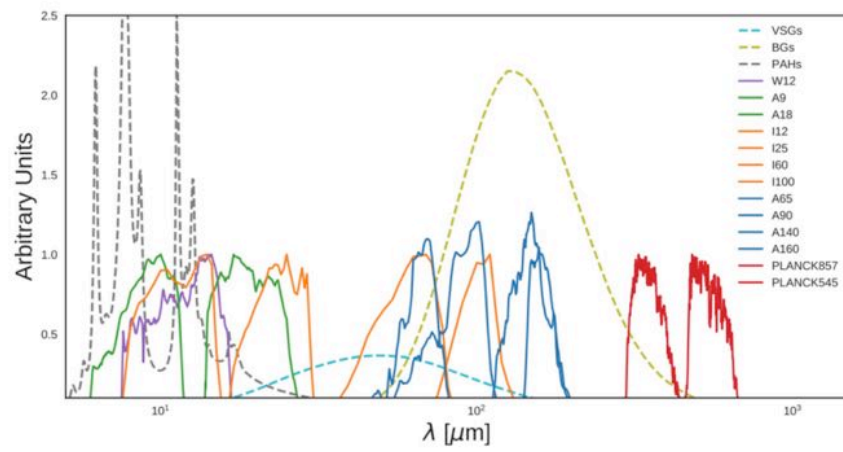
Werner, M. W. et al. (2004). "The Spitzer Space Telescope Mission." *The Astrophysical Journal Supplement Series* **154**: 1-9.

Wright, E.L. et al. (2010). "The Wide-field Infrared Survey Explorer (WISE): Mission Description and Initial On-orbit Performance." *The Astronomical Journal* **140**: 1868-1881.

Viana, A. et al. (2009). *NICOS Instrument Handbook, Version 11.0*, Space Telescope Institute.

Example of a multi-wavelength study using archive data.

A = AKARI
I = IRAS
P = Planck



From: Bell, A. (Ph.D. thesis, 2018)

Ref: Bell, A. 2018, "Investigation of Interstellar Dust Emission in the Infrared-Microwave Range with All-sky Surveys", Ph.D. thesis, Univ. of Tokyo.

end